

## Effect of magnetization inhomogeneity on magnetic microtraps for atoms

S. Whitlock, B. V. Hall,\* T. Roach, R. Anderson, M. Volk, P. Hannaford, and A. I. Sidorov  
*ARC Centre of Excellence for Quantum-Atom Optics and Centre for Atom Optics and Ultrafast Spectroscopy,  
 Swinburne University of Technology, Hawthorn, Victoria 3122, Australia*

(Received 2 May 2006; revised manuscript received 11 February 2007; published 2 April 2007)

We report on the origin of fragmentation of ultracold atoms observed on a magnetic film atom chip. Radio frequency spectroscopy and optical imaging of the trapped atoms is used to characterize small spatial variations of the magnetic field near the film surface. Direct observations indicate the fragmentation is due to a corrugation of the magnetic potential caused by long range inhomogeneity in the film magnetization. A model which takes into account two-dimensional variations of the film magnetization is consistent with the observations.

DOI: [10.1103/PhysRevA.75.043602](https://doi.org/10.1103/PhysRevA.75.043602)

PACS number(s): 03.75.Be, 39.25.+k, 07.55.Ge, 34.50.Dy

### I. INTRODUCTION

An atom chip is designed to manipulate magnetically trapped ultracold atoms near a surface using an arrangement of microfabricated wires or patterned magnetic materials [1,2]. Since the realization of Bose-Einstein condensates (BECs) on atom chips [3,4], pioneering experiments have studied single-mode propagation along waveguides [5], transport and adiabatic splitting of a BEC [6] and recently on-chip atom interferometry [7,8]. Permanent magnets are particularly attractive for atom chips as they can provide complex magnetic potentials [9] while suppressing current noise that causes heating and limits the lifetime of trapped atoms near a surface [10]. To date, permanent magnet atom chips have been developed with a view to study one-dimensional quantum gases [11–13], decoherence of BEC near surfaces [10,14], hybrid magnetic and optical trapping configurations [15], and self-biased fully permanent magnetic potentials [16]. It has been found, however, that in addition to current noise, atom chips have other limitations, as undesired spatial magnetic field variations associated with the current-carrying wires or magnetic materials can act to fragment the trapped atoms.

In previous work, fragmentation of atoms trapped near current-carrying wires was traced to roughness of the wire edges that causes tiny current deviations [17,18]. This introduces a spatially varying magnetic field component parallel to the wire which corrugates the bottom of the trap potential. While more advanced microfabrication techniques have been used to produce wires with extremely straight edges, thereby minimizing fragmentation [19,20], the first experiments with permanent magnet atom chips have now also indicated the presence of significant fragmentation [13,21,22]. This has motivated further work towards understanding the mechanisms that cause fragmentation near magnetic materials.

In this paper we report on the origin of fragmentation near the surface of a permanent magnetic film atom chip. To characterize the magnetic field near the film surface we have developed a technique which combines precision radio frequency (rf) spectroscopy of trapped atoms with high spatial resolution optical imaging. This allows sensitive and intrin-

sically calibrated measurements of the magnetic field landscape to be made over a large area. We find the fragmentation originates from long range inhomogeneity in the film magnetization and has characteristics that differ from those observed for current-carrying wire atom chips. To account for the observations we have developed a model for the spatial decay of random magnetic fields from the surface due to inhomogeneity in the film magnetization. After the measurements using the ultracold atoms we have studied the magnetic field near the chip surface using a home-built scanning magnetoresistance microscope.

### II. EXPERIMENTAL SETUP

A schematic diagram of a basic magnetic film atom chip is shown in Fig. 1. Our atom chip uses a  $\text{Tb}_6\text{Gd}_{10}\text{Fe}_{80}\text{Co}_4$  film which exhibits strong perpendicular anisotropy [14]. The edge of the  $300\ \mu\text{m}$  thick glass-slide substrate is polished to optical quality prior to film deposition. Scanning profilometer measurements on similarly prepared substrates indicate that the residual edge roughness is less than 50 nm and the top surface is extremely smooth. The substrate is sputter coated with a multilayer magnetic film ( $6 \times 150\ \text{nm}$   $\text{Tb}_6\text{Gd}_{10}\text{Fe}_{80}\text{Co}_4$  and  $6 \times 140\ \text{nm}$  Cr) and a gold overlayer (100 nm), and the film topology accurately follows that of the polished substrate. The deposited film has been analyzed using a SQUID magnetometer and a magnetic force microscope (MFM) and has shown excellent magnetic properties [23]. The film is magnetized perpendicular to the surface by

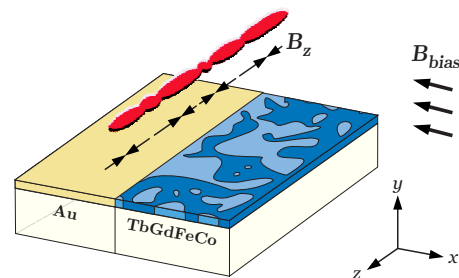


FIG. 1. (Color online) Schematic diagram of our permanent magnetic film atom chip. Long range inhomogeneity in the film magnetization leads to fragmentation of the trapped cloud of ultracold atoms when positioned near the surface.

\*Electronic address: [brhall@swin.edu.au](mailto:brhall@swin.edu.au)

a magnetic field of 1 T and afterwards is magnetically homogeneous within the sensitivity of the MFM. A second glass slide, coated with a nonmagnetic gold film, completes the reflective atom chip surface (Fig. 1). Both substrates are then epoxied to a 500  $\mu\text{m}$  thick silver foil current-carrying structure which is used for loading ultracold atoms into the permanent magnet microtrap, to provide weak longitudinal confinement, and as an in-built radio frequency antenna.

At the edge of the perpendicularly magnetized film a field is produced that is analogous to that of a thin current-carrying wire aligned with the film edge ( $I_{\text{eff}}=0.2$  A) [9,14]. A magnetic microtrap is formed by the field from the film, a uniform magnetic field  $B_{\text{bias}}$ , and two current-carrying end wires.

In the experiment  $2 \times 10^8$   $^{87}\text{Rb}$  atoms are collected in a mirror magneto-optical trap located 5 mm from the surface. These atoms are optically pumped to the  $|F=2, m_F=+2\rangle$  hyperfine state and subsequently transferred to a magnetic trap formed by a Z-shaped current-carrying wire and  $B_{\text{bias}}$ . A preliminary rf evaporative cooling stage is used to reduce the cloud temperature below 5  $\mu\text{K}$ . The remaining atoms are then transferred to the magnetic film microtrap by adiabatically reducing the current through the Z-shaped wire to zero.

The final values of  $B_{\text{bias}}$  vary from 0.2 mT to 0.8 mT, so the transverse trap frequency  $\omega_r$  varies between  $2\pi \times 410$  Hz and  $2\pi \times 1500$  Hz while the trap position  $y_0$  ranges from 200  $\mu\text{m}$  to 50  $\mu\text{m}$  from the film edge. The end wires are operated at 0.5 A such that the trap depth is  $\sim 100$   $\mu\text{K}$  and the elongated cloud of atoms extends 5 mm along the edge of the atom chip to allow measurement of the magnetic potential.

### III. SPATIALLY RESOLVED RADIO FREQUENCY SPECTROSCOPY

The narrow energy distribution of ultracold atoms is an inherent advantage when used as a probe of weak potentials. In particular, the equilibrium distribution of trapped atoms has been used to image magnetic fields near test wires with high sensitivity and high spatial resolution [24,25]. In parallel, rf spectroscopy has been used as a precise and powerful method for investigating the properties of cold atom clouds [26–30]. In this paper we use rf spectroscopy of ultracold atoms to accurately profile small magnetic field variations near the magnetic film surface.

#### A. Measurement technique

A spatially uniform rf field of frequency  $\nu$  is applied perpendicular to the trap axis to resonantly outcouple atoms to untrapped magnetic states at positions where  $g_F \mu_B |B(x, y, z)| = h\nu$ . The rf field is swept using a single frequency ramp ( $\sim 0.2$  MHz/s) from 2 MHz to a final cutoff frequency  $\nu_f$  ranging between 1.4 MHz and 0.5 MHz. The Rabi frequency of the rf transition is  $2\pi \times 0.5$  kHz, high enough to ensure that atoms with total energy greater than  $h\nu$  are removed from the trap with high probability and that regions of the potential where  $g_F \mu_B |B(x, y, z)| \geq h\nu$  thereafter remain unpopulated. During the early stages of the rf

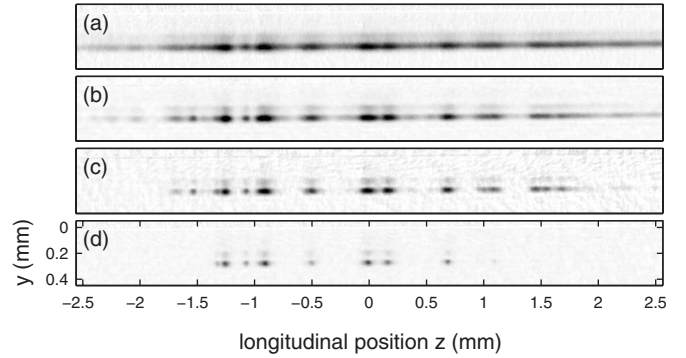


FIG. 2. Absorption images of the  $^{87}\text{Rb}$  atomic density in the magnetic microtrap located  $y_0=67$   $\mu\text{m}$  below the magnetic film edge. The trap parameters are  $B_{\text{bias}}=0.57$  mT,  $B_0=82$   $\mu\text{T}$ , and  $\omega_r=2\pi \times 1070$  Hz. The initial cloud temperature is  $T=10$   $\mu\text{K}$ . As the rf cutoff  $\nu_f$  is decreased, the structure of the potential is revealed, (a)  $\nu_f=1238$  kHz, (b)  $\nu_f=890$  kHz, (c)  $\nu_f=766$  kHz, (d)  $\nu_f=695$  kHz.

sweep the cloud undergoes some evaporative cooling as the in-trap collision rate is high enough to allow rethermalization. At the end of the sweep the resonant frequency approaches that corresponding to the trap bottom and the cloud becomes significantly truncated by the rf field.

Immediately after the sweep,  $B_{\text{bias}}$  is switched off within 0.5 ms to accelerate the atoms away from the film surface for 1 ms in the remaining permanent magnetic field gradient. The rapid switch off also causes some nonadiabatic transitions to the  $m_F=+1$  state, the presence of which can be seen in Fig. 2 as shadows above the main absorption images. The  $m_F=+1$  components are excluded from the analysis. The longitudinal density distribution is unperturbed during the expansion and is an accurate representation of the in-trap distribution. A resonant absorption image is then recorded by a CCD with a spatial resolution of 5  $\mu\text{m}$ . A series of absorption images for different values of  $\nu_f$  is shown in Fig. 2. Noticeable fragmentation is observed when  $\nu_f$  is reduced below 1.3 MHz [Fig. 2(a)]. For  $\nu_f \sim 0.9$  MHz the density distribution becomes truncated by the rf field and regions of the atomic density decrease to zero [Fig. 2(b)]. Reducing  $\nu_f$  further results in well separated clumps of atoms which are found only in the lowest potential wells [Figs. 2(c) and 2(d)].

#### B. Data analysis

For a quantitative analysis we assume that the full trapping potential can be expressed in terms of the transverse confinement and the corrugated longitudinal potential  $m_F g_F \mu_B |B_z(z) + B_0|$  where  $B_0$  is a uniform offset field [18]. The atomic distribution in the trap immediately after the rf sweep is described by a truncated Boltzmann distribution [27,31]. To extract  $|B_z(z) + B_0|$ , the integrated atomic density as a function of  $\nu_f$  can be fit for each position  $z$  to the truncated thermal distribution function

$$n(z, \beta) = n_\infty(z) [\text{erf}(\sqrt{\beta}) - 2\sqrt{\beta/\pi} e^{-\beta} (1 + 2\beta/3)], \quad (1)$$

where  $n_\infty$  is the integrated atom density before truncation and the spatially dependent truncation parameter  $\beta$  is

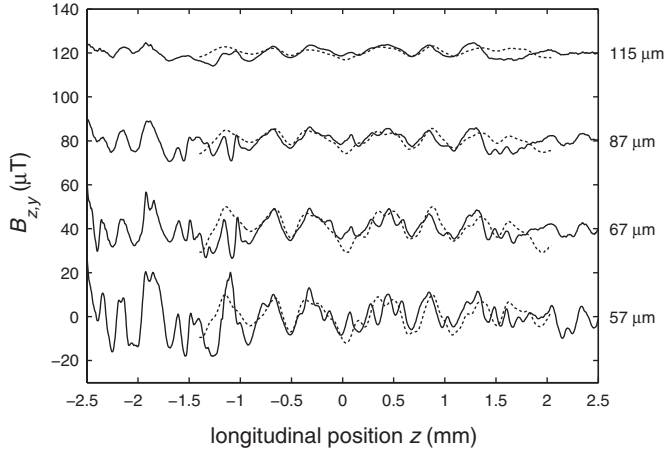


FIG. 3. Magnetic field profiles  $B_z(z)$  measured using spatially resolved rf spectroscopy (solid lines) for various distances  $y_0$  below the magnetic film edge. The field offset  $B_0$  and the effect of weak longitudinal confinement are subtracted and each profile has been offset by  $40 \mu\text{T}$  for clarity. The dotted lines correspond to measurements of the magnetic film edge using a scanning magnetoresistance probe which measures the  $B_y$  component of the corrugated magnetic field. The relative longitudinal offset between the two measurements is initially unknown and is adjusted for optimum agreement.

$$\beta(z, \nu_f) = [m_F h \nu_f - m_F g_F \mu_B |B_z(z) + B_0|] / k_B T, \quad (2)$$

where  $T$  is a fit parameter, which characterizes the nonequilibrium distribution during truncation. We find however that this model does not satisfactorily reproduce the density distribution in regions of the potential where the atomic density becomes large; specifically at the bottom of each potential well for lower values of  $\nu_f$ . To minimize this effect we section the full data set into  $80 \mu\text{m}$  spatial regions and fit Eq. (1) using a two-dimensional minimization algorithm as opposed to fitting for each value of  $z$  independently. This effectively constrains the fitted truncation temperature  $T$  to vary smoothly over a range corresponding roughly to the extent of a potential well. After reconstructing the magnetic field profile the effect of the end wires is subtracted. The statistical uncertainty in the measurement is approximately  $0.1 \mu\text{T}$ , which is mainly attributed to fluctuations of external magnetic fields. With appropriate magnetic shielding the expected sensitivity of the technique is limited by the power broadened rf linewidth required to effectively outcouple atoms.

Complete magnetic field profiles are given for four distances from the film edge in Fig. 3. First, the amplitude and structure of the observed corrugated potential are constant from day to day; however the rms amplitude increases as the trap is positioned closer to the surface, following an approximate power-law dependence given by  $B_{z,\text{rms}} = 1.05 \times 10^{-7} y_0^{-1.85} \mu\text{T}$ . The figure of merit for corrugation observed above the  $\text{Tb}_6\text{Gd}_{10}\text{Fe}_{80}\text{Co}_4$  film is  $B_{z,\text{rms}}/B(y_0) = 6 \times 10^{-3}$  for a distance of  $y_0 = 115 \mu\text{m}$  or  $B_{z,\text{rms}}/B(y_0) = 1.2 \times 10^{-2}$  for  $y_0 = 57 \mu\text{m}$ . Extrapolation of our data also allows us to estimate the amplitude of the corrugated potential for closer approaches. For a distance of  $y_0 = 10 \mu\text{m}$  we expect

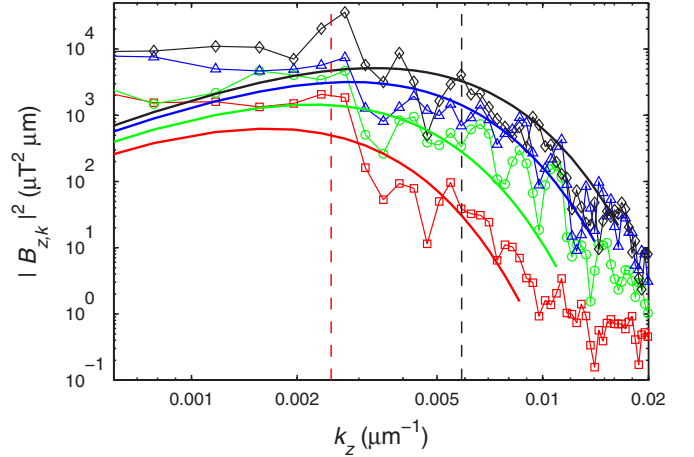


FIG. 4. (Color online) Spectral density of the magnetic field variations for different distances from the film edge. The points represent experimental data with (squares)  $y_0 = 115 \mu\text{m}$ , (circles)  $y_0 = 87 \mu\text{m}$ , (triangles)  $y_0 = 67 \mu\text{m}$ , and (diamonds)  $y_0 = 57 \mu\text{m}$ . The vertical dashed lines correspond to the characteristic wave vectors  $k = 1/390 \mu\text{m}^{-1}$  and  $k = 1/170 \mu\text{m}^{-1}$  for the  $y_0 = 115 \mu\text{m}$  and  $y_0 = 57 \mu\text{m}$  data sets, respectively. The solid lines represent the expected noise due to white noise variations of the film magnetization given by Eq. (4).

the relative strength of the corrugation to be  $B_{z,\text{rms}}/B(y_0) \approx 5 \times 10^{-2}$ . This is significantly higher than  $B_{z,\text{rms}}/B(y_0) \sim 10^{-5}$  observed for the same distance using evaporatively deposited microwires [19], highlighting the need for further improvement of the properties of magnetic materials.

We also analyze the frequency characteristics of the corrugated magnetic potentials. Figure 4 shows the power spectral density of each profile estimated using Welch's averaged modified periodogram method with eight segments overlapping by 50% [32]. The spectra reach a maximum for low wave vectors and roll off at a value of  $k_z$  which depends on the distance to the film edge. From this we identify a characteristic period, which for  $y_0 > 100 \mu\text{m}$  corresponds to about  $390 \mu\text{m}$ , significantly longer than that commonly observed near electroplated wires [18,33]. Fourier components with shorter periods contribute less than 10% to the total integrated noise power. Additional corrugations appear closer to the film ( $y_0 < 70 \mu\text{m}$ ) and the characteristic period is about  $170 \mu\text{m}$ . These  $y$ -dependent characteristics of the potential have allowed time-dependent manipulation of BECs in a double-well region of the corrugated potential [34].

We have found that the amplitude of the corrugated potential is not consistent with magnetostatic calculations based on fluctuations of the film edge (Fig. 6), suggesting that the cause of fragmentation may be spatial variations of the magnetization within the body of the film. To investigate this, a second bias field is applied in the  $y$  direction to bring the trap closer to the surface while keeping a constant distance from the edge of the magnetic film. Two CCD cameras and two resonant probe laser beams are used to simultaneously record absorption images parallel and perpendicular to the trap axis to measure the transverse position  $x$  of the cloud and the longitudinal  $z$  profile of the cloud in equilibrium with the trapping potential (Fig. 5). When the cloud of atoms is posi-

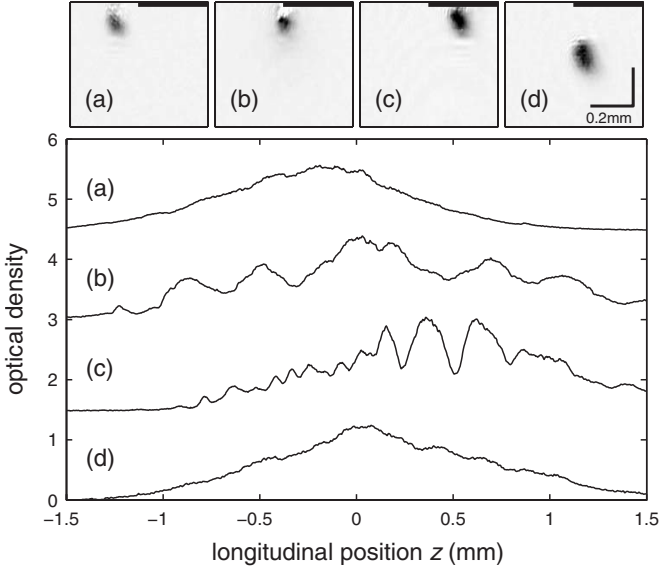


FIG. 5. Transverse absorption images and longitudinal absorption cross sections of trapped thermal clouds of atoms positioned (a)  $y_0=50 \mu\text{m}$ ,  $x_0=-100 \mu\text{m}$ , below the nonmagnetic gold surface; (b)  $y_0=50 \mu\text{m}$ ,  $x_0=0 \mu\text{m}$ , directly below the film edge; (c)  $y_0=50 \mu\text{m}$ ,  $x_0=100 \mu\text{m}$ , below the magnetic film surface; and (d)  $y_0=100 \mu\text{m}$ ,  $x_0=0 \mu\text{m}$ , below the film edge. The solid lines in the absorption images indicate the approximate position of the magnetic film. Each optical density cross section is offset by 1.5 for clarity.

tioned  $y_0=50 \mu\text{m}$  from the surface of the magnetic film ( $x_0=+100 \mu\text{m}$ ) we observe significant fragmentation [Fig. 5(c)]. A similarly prepared cloud positioned  $y_0=50 \mu\text{m}$  from the nonmagnetic gold surface ( $x_0=-100 \mu\text{m}$ ) for the same distance to the film edge, however, does not exhibit significant atomic density variations [Fig. 5(a)]. The radial trap frequency for both situations is approximately  $\omega_r=2\pi \times 400 \text{ Hz}$  and the cloud temperature is kept constant at  $\sim 5 \mu\text{K}$ . The central positions  $z$  of the clouds are offset due to the axial confining potential produced by the end wires which is affected by the applied  $y$  bias field. In addition to the clear difference in the fragmentation amplitude, we also note that the relative locations of the maxima and minima differ for atom clouds below the magnetic film surface [Fig. 5(c)] compared with the one directly below the edge [Fig. 5(b)]. These observations confirm that the magnetic field variations originate from the magnetic material itself and not from imperfections along the edge of the film.

#### IV. MAGNETIZATION MODEL

Our model describes the effect of two-dimensional spatial variations in the perpendicular magnetization  $M_y(x, z)$  of the film. Inhomogeneity leads to the appearance of a random magnetic field above the surface, of which we are most interested in the magnetic field component  $B_z(x, y, z)$  that corrugates the bottom of the trapping potential. Using a standard approach incorporating the two-dimensional Fourier transform of the random magnetization  $N(k_x, k_z)$  and the magnetic

scalar potential we obtain an expression for the  $B_z$  component of the corrugated magnetic field. In the case of a magnetic film occupying a half-plane with the edge at  $x=0$  (Fig. 1 and arbitrary magnetization noise we have, for heights greater than the film thickness,

$$B_z = i2\pi\mu_0 y \delta \int_{-\infty}^{\infty} \int_{-\infty}^{\infty} dk_x dk_z k_z^2 N(k_x, k_z) e^{i2\pi(k_x x + k_z z)} \times \int_{-x}^{\infty} dx' e^{i2\pi k_x x'} \frac{K_1(2\pi k_z \sqrt{x'^2 + y^2})}{\sqrt{x'^2 + y^2}}, \quad (3)$$

where  $\delta$  is the film thickness and  $K_1$  is the modified Bessel function of the second kind. In general this expression can be used to describe any planar pattern of elements that can be represented as a linear combination of step functions. For white noise fluctuations in the magnetization ( $|N(k_x, k_z)| = |N_0|$ ) the rms value of the magnetic field roughness as a function of distance from the edge can be evaluated analytically. We calculate the magnetic field amplitude squared and perform ensemble averaging to obtain the expected height dependence of the magnetic field noise. The field noise spectrum above the edge can then be evaluated and is given by

$$|B_{z,k}(k_z, y)|^2 = \pi^2 \mu_0^2 \delta^2 |N_0|^2 k_z^3 K_1(4\pi k_z y), \quad (4)$$

where a comparison between the data and the model (Fig. 4) indicates  $|N_0|=0.36 \text{ Am}$ . The model is in good agreement with the experimental data for  $k_z > 0.002 \mu\text{m}^{-1}$ , however at low wave vectors we observe a systematic deviation which could be explained by additional long range variations in the film magnetization on the mm length scale. We note that these components provide a minor contribution to the overall rms magnetic field noise for the distances of interest ( $y_0 < 200 \mu\text{m}$ ) and do not affect our general results.

Finally we obtain an expression for the rms amplitude  $B_{z,\text{rms}}$  of the field noise which includes the dependence across the film edge,

$$B_{z,\text{rms}} = \sqrt{\frac{3}{\pi} \frac{\mu_0 d \delta \Delta M}{16y^2}} \sqrt{1 + \frac{15}{8} \alpha - \frac{5}{4} \alpha^3 + \frac{3}{8} \alpha^5}, \quad (5)$$

where  $\alpha = x/\sqrt{x^2 + y^2}$ ,  $\Delta M$  is the rms magnetization inhomogeneity and  $d$  is the characteristic feature size of the domain structure. For  $x=0$  the model predicts that the corrugated magnetic field component decays with a  $y^{-2}$  dependence, consistent with our experimental result of  $y^{-1.85 \pm 0.3}$ . This behavior can also be compared with the more rapid decay ( $\propto y^{-2.5}$ ) expected for white noise fluctuations of the edge of current-carrying wires [17,18]. Film edge fluctuations are expected to produce corrugations three orders of magnitude smaller than that observed in the experiments (Fig. 6). The model also predicts the fast decay of the corrugated magnetic field away from the film edge for  $x < 0$  (Fig. 6 inset).

In Fig. 6 the experimental results are compared with the model with relevant energy scales indicated by dotted lines. The characteristic feature size and distribution function of the domain structure has been inferred from MFM measurements of a demagnetized  $\text{Tb}_6\text{Gd}_{10}\text{Fe}_{80}\text{Co}_4$  film and is found to have close to white noise characteristics with  $d \approx 5 \mu\text{m}$ .

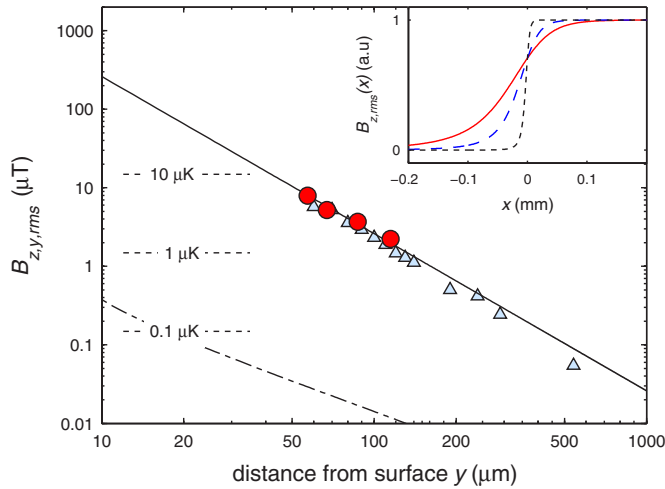


FIG. 6. (Color online) Behavior of the magnetic field roughness  $B_{z,rms}$  measured using rf spectroscopy of ultracold atoms (circles) and  $B_{y,rms}$  measured using a scanning magnetoresistive probe (triangles), as a function of distance from the film surface. The dashed line corresponds to the expected noise for a homogeneously magnetized film with a measured edge roughness of 50 nm. The solid line is a fit to the results of rf spectroscopy using Eq. (5) with a characteristic feature size  $d=5 \mu\text{m}$  and  $\Delta M/M_s \approx 0.3$ . The inset shows the predicted  $x$  dependence of the field roughness away from the film edge for distances of  $y_0=10 \mu\text{m}$  (dotted),  $y_0=50 \mu\text{m}$  (dashed), and  $y_0=100 \mu\text{m}$  (solid line).

The best fit of Eq. (5) to the data is found for  $\Delta M/M_s \approx 0.3$ , where  $M_s$  is the saturation magnetization of the film. If the inhomogeneity is assumed to originate from reversal of a small number of magnetic domains [ $M_y(x,z) = \pm M_s$ ] then we conclude that the mean magnetization of the film is greater than  $0.9M_s$ .

## V. MAGNETORESISTANCE MICROSCOPY

After the rf spectroscopy measurements of the corrugated potential we have removed the atom chip from the vacuum chamber and have performed additional characterization using a magnetoresistance microscope which is sensitive to the out-of-plane  $B_y$  field component [35,36]. Our home-built magnetoresistance microscope [37] incorporates a commercially available magnetic tunnel junction probe (MicroMagnetics STJ-020) which allows approach distances of  $\sim 10 \mu\text{m}$ . The noise levels for our measurements are about  $0.1 \mu\text{T}$  and the spatial resolution is approximately  $50 \mu\text{m}$ . Figure 3 shows a series of magnetic field profiles recorded using the magnetoresistance microscope at the heights which correspond to those of the rf spectroscopy results. The relative longitudinal offset of the magnetoresistance measurements is initially unknown and has been adjusted for optimal agreement with the results of rf spectroscopy. We note that

the rms amplitude and the spectral characteristics of the two independent measurements as a function of height above the film edge are very similar.

From our model it is also possible to predict the field noise dependence for the  $B_{y,rms}$  component at  $x=0$ , which is simply related to the  $B_{z,rms}$  component by  $B_{y,rms}(y) = \sqrt{2}B_{z,rms}(y)$ , allowing a direct comparison between the results obtained using the magnetoresistance microscope and those obtained using rf spectroscopy of ultracold atoms. Shown in Fig. 6 (triangles) are additional measurements of the rms field noise measured between  $60 \mu\text{m}$  and  $500 \mu\text{m}$  from the magnetic film edge. These are also consistent with the  $y^{-2}$  power-law spatial decay, where the small systematic discrepancy between the two measurement methods can be attributed to a  $20 \mu\text{m}$  transverse displacement of the magnetoresistance probe from the film edge.

## VI. CONCLUSION

The  $\text{Tb}_6\text{Gd}_{10}\text{Fe}_{80}\text{Co}_4$  magnetic film was originally chosen for its desirable magnetic properties including a large coercivity ( $\mu_0 H_c = 0.32 \text{ T}$ ) and a high Curie temperature ( $T_c \sim 300 \text{ }^\circ\text{C}$ ) [23]. We attribute the observed inhomogeneity to deterioration of the magnetic film experienced during the vacuum bake-out ( $140 \text{ }^\circ\text{C}$  over 4 days) despite the relatively high Curie temperature of our film. This conclusion is consistent with reports of reduced perpendicular anisotropy found for similar films after annealing at temperatures above  $100 \text{ }^\circ\text{C}$  [38,39] and with our own measurements on similar films. After our magnetoresistance studies we have remagnetized the film thereby reducing the level of inhomogeneity by approximately a factor of 10.

In conclusion, trapped ultracold atoms are very sensitive to small magnetic field variations found near the surface of the permanent magnetic film. These variations corrugate the longitudinal trapping potential and result in fragmentation of atomic density. We have developed the technique of spatially resolved rf spectroscopy as a powerful method for accurately mapping small magnetic field variations near the surface of the magnetic film. A simple model accounts for spatial inhomogeneity of the film magnetization and agrees well with the observations. The development of permanent magnet atom chips will require additional research aimed at further optimizing the quality of the magnetic films.

## ACKNOWLEDGMENTS

The authors would like to thank J. Wang for the deposition of the magnetic film. One of the authors (T.R.) acknowledges the Donors of the American Chemical Society Petroleum Research Fund for support during this research. This project is supported by the ARC Centre of Excellence for Quantum-Atom Optics and a Swinburne University Strategic Initiative grant.

- [1] R. Folman, P. Krüger, J. Schmiedmayer, J. Denschlag, and C. Henkel, *Adv. At., Mol., Opt. Phys.* **48**, 263 (2002).
- [2] J. Fortágh and C. Zimmermann, *Rev. Mod. Phys.* **79**, 235 (2007).
- [3] W. Hänsel, P. Hommelhoff, T. W. Hänsch, and J. Reichel, *Nature (London)* **413**, 498 (2001).
- [4] H. Ott, J. Fortágh, G. Schlotterbeck, A. Grossmann, and C. Zimmermann, *Phys. Rev. Lett.* **87**, 230401 (2001).
- [5] A. E. Leanhardt, A. P. Chikkatur, D. Kielpinski, Y. Shin, T. L. Gustavson, W. Ketterle, and D. E. Pritchard, *Phys. Rev. Lett.* **89**, 040401 (2002).
- [6] P. Hommelhoff, W. Hänsel, T. Steinmetz, T. W. Hänsch, and J. Reichel, *New J. Phys.* **7**, 3 (2005).
- [7] Y. Shin, C. Sanner, G. B. Jo, T. A. Pasquini, M. Saba, W. Ketterle, D. E. Pritchard, M. Vengalattore, and M. Prentiss, *Phys. Rev. A* **72**, 021604(R) (2005).
- [8] T. Schumm, S. Hofferberth, L. M. Andersson, S. Wildermuth, S. Groth, I. Bar-Joseph, J. Schmiedmayer, and P. Krüger, *Nature (London)* **1**, 57 (2005).
- [9] A. I. Sidorov, R. J. McLean, F. Scharnberg, D. S. Gough, T. J. Davis, B. A. Sexton, G. I. Opat, and P. Hannaford, *Acta Phys. Pol. B* **33**, 2137 (2002).
- [10] C. D. J. Sinclair, E. A. Curtis, I. L. Garcia, J. A. Retter, B. V. Hall, S. Eriksson, B. E. Sauer, and E. A. Hinds, *Phys. Rev. A* **72**, 031603(R) (2005).
- [11] M. Vengalattore, R. S. Conroy, W. Rooijakkers, and M. Prentiss, *J. Appl. Phys.* **95**, 4404 (2004).
- [12] I. Llorente-Garcia, C. D. J. Sinclair, E. A. Curtis, S. Eriksson, B. E. Sauer, and E. A. Hinds, *J. Phys.: Conf. Ser.* **19**, 70 (2005).
- [13] M. Boyd, E. W. Streed, P. Medley, G. K. Campbell, J. Mun, W. Ketterle, and D. E. Pritchard, e-print cond-mat/0608370.
- [14] B. V. Hall, S. Whitlock, F. Scharnberg, P. Hannaford, and A. Sidorov, *J. Phys. B* **39**, 27 (2006).
- [15] A. Jaakkola, A. Shevchenko, K. Lindfors, M. Hautakorpi, E. Il'yashenko, T. H. Johansen, and M. Kaivola, *Eur. Phys. J. D* **35**, 81 (2005).
- [16] I. Barb, R. Gerritsma, Y. T. Xing, J. B. Goedkoop, and R. J. C. Spreeuw, *Eur. Phys. J. D* **35**, 75 (2005).
- [17] D. W. Wang, M. D. Lukin, and E. Demler, *Phys. Rev. Lett.* **92**, 076802 (2004).
- [18] J. Estève, C. Aussibal, T. Schumm, C. Figl, D. Maily, I. Bouchoule, C. I. Westbrook, and A. Aspect, *Phys. Rev. A* **70**, 043629 (2004).
- [19] P. Krüger, L. M. Andersson, S. Wildermuth, S. Hofferberth, E. Haller, S. Aigner, S. Groth, I. Bar-Joseph, and J. Schmiedmayer, e-print cond-mat/0504686.
- [20] L. D. Pietra, S. Aigner, C. vom Hagen, H. J. Lezec, and J. Schmiedmayer, *J. Phys.: Conf. Ser.* **19**, 30 (2005).
- [21] C. D. J. Sinclair, J. A. Retter, E. A. Curtis, B. V. Hall, I. Llorente-Garcia, S. Eriksson, B. E. Sauer, and E. A. Hinds, *Eur. Phys. J. D* **35**, 105 (2005).
- [22] B. V. Hall, S. Whitlock, F. Scharnberg, P. Hannaford, and A. Sidorov, in *Laser Spectroscopy XVII*, edited by E. A. Hinds, A. Ferguson, and E. Riis (World Scientific, Singapore, 2005).
- [23] J. Y. Wang, S. Whitlock, F. Scharnberg, D. Gough, A. I. Sidorov, R. J. McLean, and P. Hannaford, *J. Phys. D* **38**, 4015 (2005).
- [24] S. Wildermuth, S. Hofferberth, I. Lesanovsky, E. Haller, L. M. Andersson, S. Groth, I. Bar-Joseph, P. Krüger, and J. Schmiedmayer, *Nature (London)* **435**, 440 (2005).
- [25] A. Günther, M. Kemmler, S. Kraft, C. J. Vale, C. Zimmermann, and J. Fortágh, *Phys. Rev. A* **71**, 063619 (2005).
- [26] A. G. Martin, K. Helmerson, V. S. Bagnato, G. P. Lafyatis, and D. E. Pritchard, *Phys. Rev. Lett.* **61**, 2431 (1988).
- [27] K. Helmerson, A. G. Martin, and D. E. Pritchard, *J. Opt. Soc. Am. B* **9**, 483 (1992).
- [28] I. Bloch, T. W. Hänsch, and T. Esslinger, *Phys. Rev. Lett.* **82**, 3008 (1999).
- [29] S. Gupta, Z. Hadzibabic, M. W. Zwierlein, C. A. Stan, K. Dieckmann, C. H. Schunck, E. G. M. van Kempen, B. J. Verhaar, and W. Ketterle, *Science* **300**, 1723 (2003).
- [30] C. Chin, M. Bartenstein, A. Altmeyer, S. Riedl, S. Jochim, J. H. Denschlag, and R. Grimm, *Science* **305**, 1128 (2004).
- [31] O. J. Luiten, M. W. Reynolds, and J. T. M. Walraven, *Phys. Rev. A* **53**, 381 (1996).
- [32] P. D. Welch, *IEEE Trans. Audio Electroacoust.* **AU-15**, 70 (1967).
- [33] J. Fortágh, H. Ott, S. Kraft, A. Günther, and C. Zimmermann, *Phys. Rev. A* **66**, 041604(R) (2002).
- [34] B. V. Hall, S. Whitlock, R. Anderson, P. Hannaford, and A. I. Sidorov, *Phys. Rev. Lett.* **98**, 030402 (2007).
- [35] S. Y. Yamamoto and S. Schultz, *Appl. Phys. Lett.* **69**, 3263 (1996).
- [36] B. D. Schrag and G. Xiao, *Appl. Phys. Lett.* **82**, 3272 (2003).
- [37] M. Volk, S. Whitlock, B. Hall, and A. I. Sidorov (unpublished).
- [38] F. E. Luborsky, *J. Appl. Phys.* **57**, 3592 (1985).
- [39] Y. J. Wang and Q. W. Leng, *Phys. Rev. B* **41**, 651 (1990).